ISSN: 2996-2544

Research Article

Journal of Research and Education

Simulation of Wake Effects Applying CFD Technique to the K-E Model

Carlos Armenta-Deu*, Raul Fernandez and Jorge Contreras

Faculty of Physics, Complutense University of Madrid, 28040 Madrid (Spain)

***Corresponding Author**
Carlos Armenta-Deu, Faculty of Physics. Complutense University of Madrid, 28040 Madrid (Spain).

Submitted: 2025, May 25; **Accepted:** 2025, Jun 27; **Published:** 2025, Jun 30

Citation: Armenta-Deu, C., Fernandez, R., Contreras, J. (2025). Simulation of Wake Effects Applying CFD Technique to the K-E Model. *J Res Edu, 3*(2), 01-12.

Abstract

In this work, we develop a simulation study on the wake effects in turbulent fluid regimes using CFD techniques to the k-ε model. We apply the k-ε model to solve the Navier-Stokes equations, capturing the most relevant parameters affecting the performance of the turbulent fluid when wake effects occur. The study focuses on the kinetic energy and energy dissipation rate, modeling the wake-time evolution to obtain its spatial distribution. The modeling and simulation produce a detailed wake velocity profile, which is critical in determining the wake impact on downstream elements. The simulation results evaluation applies to improve the design of energy use downstream systems by minimizing energy losses and improving efficiency. The study applies to rotating obstacles but is valid for other fluid applications.

Keywords: Turbulent fluid, Wakes, CFD technique, Modelling Simulation, Fluid stream performance, Turbulent kinetic energy

1. Introduction

The study and analysis of rotational wake effects are critical to evaluate the influence of fluid turbulent regimes on downstream systems or devices, which may cause mechanical damages and energy losses, reducing the system or device performance and increasing the risk of breakage. Systems designed to operate under a laminar regime suffer from increased drag forces due to the mechanical interaction with turbulent fluid [1]. These drag forces increase mechanical wear and reduce energy efficiency therefore, a deep knowledge of rotational wake time evolution and spatial distribution is mandatory to evaluate the possible damages and fluid available power [2,3].

The analysis of turbulent fluid performance is developed using the Navier-Stokes equations due to the mathematical complexity of the problem [4]. Navier-Stokes equations, however, do not provide numerical but analytical solutions to solve the mathematical problem [5]. In fluid mechanics, we cannot solve most practical problems by applying analytical solutions due to the limitations in planning the problem [6], requiring approximations or computing techniques [7]. This last option represents a solid approach to numerical solutions due to its capacity to simulate the system's current configuration [8].

Among the computing techniques for solving Navier-Stokes equations, CFD is revealed as the most practical because it can reproduce fluid performance with high accuracy and the associated programs and libraries, helping the CFD solver analyze the problem and achieve an exact solution [9-13].

The application of Navier-Stokes equations to Fluid Mechanics covers many systems and configurations; in this work, we focus on the aerodynamic structure of wind turbine blades and the effects that turbulent flow created by turbine rotor downstream rotational wakes have on the nearby turbines.

2. Theoretical Foundations

Fluid properties and chaotic performance characterize a turbulent regime. The easiest way to face the problem is decomposing the liquid velocity in an average value, U, and a fluctuant term depending on time, u'(t). In this way, we can define the fluid properties by combining the average and statistical variation values. If we apply the Reynolds decomposition to the fluid velocity, u(t), we have:

$$u(t) = U + u'(t) \quad (1)$$

We can apply the same decomposition procedure to any other fluid property. Therefore, we can use the Navier-Stokes equations, implementing the Reynolds' decomposition to any of the involved fluid parameters.

2.1 The k-ε Model

The k-ε model is the most widely validated process for turbulent fluids [14]. The model focuses on the mechanism affecting the kinetic energy turbulent component. Applying the Reynolds' decomposition process, the fluid kinetic energy is:

$$k(t) = K + k'(t) \tag{2}$$

The average and turbulent components are expressed as:

$$K = \frac{1}{2}\left(U^2 + V^2 + W^2\right) \tag{3}$$

$$k' = \frac{1}{2}\left(\bar{u}'^2 + \bar{v}'^2 + \bar{w}'^2\right) \tag{4}$$

U, V, and W are the Cartesian average fluid velocity components in X, Y, and Z direction, while $\bar{u}'$, $\bar{v}'$, and $\bar{w}'$ are the turbulent components.

Since the turbulent fluid generates mechanical wear, it is necessary to define the strain tensor as:

$$s_{ij} = S_{ij} + s'_{ij} \tag{5}$$

The subscripts i and j correspond to the three spatial directions; therefore, i,j=1,2,3

Considering the orthogonal components:

$$\begin{aligned} s_{xx}(t) &= S_{xx} + s'_{xx} = \frac{\partial U}{\partial x} + \frac{\partial u'}{\partial x} \\ s_{yy}(t) &= S_{yy} + s'_{yy} = \frac{\partial V}{\partial y} + \frac{\partial v'}{\partial y} \\ s_{zz}(t) &= S_{zz} + s'_{zz} = \frac{\partial W}{\partial z} + \frac{\partial w'}{\partial z} \end{aligned} \tag{6}$$

For the cross components:

$$\begin{aligned} s_{xy} &= \frac{1}{2}\left(\frac{\partial U}{\partial y} + \frac{\partial u'}{\partial y} + \frac{\partial V}{\partial x} + \frac{\partial v'}{\partial x}\right) \\ s_{xz} &= \frac{1}{2}\left(\frac{\partial U}{\partial z} + \frac{\partial u'}{\partial z} + \frac{\partial W}{\partial x} + \frac{\partial w'}{\partial x}\right) \\ s_{zy} &= \frac{1}{2}\left(\frac{\partial V}{\partial z} + \frac{\partial v'}{\partial z} + \frac{\partial W}{\partial y} + \frac{\partial w'}{\partial y}\right) \end{aligned} \tag{7}$$

We have not included the cross components s_{yx}, s_{zx}, and s_{yz} because they are symmetric, s_{ij}=s_{ji} for $i \neq j$.

Now, applying to the average kinetic energy:

$$\underbrace{\frac{\partial(\rho K)}{\partial t}}_{(I)} + \underbrace{\nabla(\rho K U)}_{(II)} = \nabla\Big(\underbrace{-pU}_{(III)} + \underbrace{2\mu U S_{ij}}_{(IV)} \underbrace{-\rho U\,\overline{u_i' u_j'}}_{(V)}\Big) \underbrace{-2\mu U S_{ij} \cdot S_{ij}}_{(VI)} + \underbrace{\rho\,\overline{u_i' u_j'}\,S_{ij}}_{(VII)} \tag{8}$$

On the other hand, the turbulent kinetic energy expression is:

$$\frac{\partial(\rho K)}{\partial t}+\nabla(\rho KU)=\nabla\left(-p'U'+2\mu U'S'_{ij}-\rho U'\overline{u_i'u_j'}\right)-2\mu U'S'_{ij}\cdot S'_{ij}+\rho\overline{u_i'u_j'}S'_{ij} \quad (9)$$

(I) (II) (III) (IV) (V) (VI) (VII)

Term (*I*) is the *k*-exchange rate, corresponding to the kinetic energy exchange rate inside the control volume. The rotational wake frame represents how the turbulent kinetic energy changes with time as the fluid flow develops and evolves along the wake path.

Term (*II*) is the *k*-convective transport, which describes the kinetic energy transportation due to the convection mechanism; in a rotational wake, it represents the way the turbulent kinetic energy evolves with the downstream fluid movement, influencing the wake length and structure.

Term (*III*) is the *k*-movement due to the pressure gradient. It represents the work done by the fluid pressure difference between two points, affecting the rotational wake spatial distribution and the interaction between turbulent flow in different regions.

Term (*IV*) is the *k*-transport by viscous effects, contributing to the rotational wake energy dissipation. It influences the wake stability and the energy transition between the different turbulent scales.

Term (*V*) is the *k*-transportation due to Reynolds forces. This term is critical for the turbulence redistribution inside the rotational wake and how it influences the fluid flow diffusion.

Term (*VI*) is the *k*-viscous dissipation, representing how the rotational wake energy dissipates into heat.

Term (*VII*) is the *k*-generation rate. This term shows the kinetic energy generation due to the interaction between Reynolds forces and speed gradient. In rotational wakes, it is a critical parameter to model the turbulent flow due to the interaction of the fluid flow and solid elements in the fluid stream and the turbulent wake development.

We can notice that the term (*VII*) is identical in Equations 8 and 9. This term is critical since it represents how the average kinetic energy converts into turbulence.

Concerning the term (*VI*), we define the dissipation coefficient as:

$$\sigma=\frac{k/m}{\varepsilon} \quad (10)$$

Analogously, we can express the Eddy viscosity as:

$$\mu_t=\rho C_\mu\frac{k^2}{\varepsilon} \quad (11)$$

The μ_t term represents the additional viscosity due to the fluid fluctuations generated by the turbulent effects, manifesting as chaotic movements at different scales.

In Equation 11, k represents the turbulent kinetic energy and ε is the energy dissipation rate. $C\mu$ is an empirical constant.

In the rotational wake's analysis, the Eddy viscosity allows us to model the fluid diffusion effects, which is critical to predict the turbulence evolution, the turbulent kinetic energy distribution, and the energy dissipation inside the rotational wake. All these effects influence the energy efficiency and the fluid interaction with solid elements in the fluid stream.

Combining all effects, we can define the transport equations as:

$$\frac{\partial(\rho k)}{\partial t}+\nabla(\rho kU)=\nabla\left(\frac{\mu_t}{\sigma_k}\nabla k\right)+2\mu_t S_{ij}\cdot S_{ij}-\rho\varepsilon \quad (12)$$

(I) (II) (III) (IV) (V)

$$\underbrace{\frac{\partial(\rho\varepsilon)}{\partial t}}_{(I)}+\underbrace{\nabla(\rho\varepsilon U)}_{(II)}=\underbrace{\nabla\left(\frac{\mu_t}{\sigma_\varepsilon}\nabla k\right)}_{(III)}+\underbrace{2C_{1\varepsilon}\frac{\varepsilon}{k}\mu_t S_{ij}\cdot S_{ij}}_{(IV)}-\underbrace{C_{2\varepsilon}\rho\frac{\varepsilon^2}{k}}_{(V)} \quad (13)$$

Terms (*I*) to (*V*) in Equations 12 and 13 mean:
(*I*): *k* or ε exchange rate
(*II*): Convection transport
(*III*): Diffusion transport
(*IV*): Energy generation
(*V*): Energy dissipation rate

The empirical constant value in Equations 12 and 13 are:

$$C_\mu = 0.09;\ \sigma_k = 1.00;\ \sigma_\varepsilon = 1.30;\ C_{1\varepsilon} = 1.44;\ C_{2\varepsilon} = 1.92 \quad (14)$$

3. Fluid Flow Velocity Profile

The velocity profile of the cross-section fluid stream depends on the duct geometric configuration through which the fluid flows and the aero or hydrodynamic characteristics, mainly the type of regime but also density, viscosity, temperature, etc.

Among the many options, we selected a Gaussian curve, representing the most frequent distribution of the cross-section velocity profile of a fluid circulating in a stream tube. The mathematical expression for this profile is [15]:

$$\frac{U}{U_\infty}=1-C(x)\exp\left(-\frac{r^2}{2\sigma_w^2(x)}\right) \quad (15)$$

The term U/U∞ represents the ratio of the wake velocity to the upstream fluid velocity far before the obstacle's plane (x=-∞). $C(x)$ is the normalized fluid velocity in the downstream x-direction, r is the radial distance from the stream tube symmetry axis, and σ_w is the standard deviation of the Gaussian distribution.

The implementation of this model implies the following premises:
• The fluid flow is incompressible, non-viscous, and operating in a steady state.
• The obstacle is a solid disk with null thickness.
• The fluid pushing power is uniform on every point of the solid disk.
• The entering fluid flow pressure recovers for all infinitesimal flows in every cell of the CFD meshing.

Applying Bernoulli's equation and imposing a linear wake expansion ($r_w \approx 2\sigma_w$), we obtain the 2D velocity profile of the Jensen model, responding to the Gaussian distribution on the cross-section of the stream tube, according to the expression:

$$\frac{U}{U_\infty}=1-A(x)\exp\left[-\frac{2}{(kx/r_a+1)^2}\left(\frac{r}{r_a}\right)^2\right] \quad (16)$$

The term r_w represents the wake radius, the distance from the stream tube symmetry axis to the point where the velocity is U_∞.

In Equation 16, k is the damping coefficient, r_a is the solid disk radius, and $A(x)$ is a coefficient defined as:

$$A(x)=\frac{2\left(1-\sqrt{1-C_T}\right)}{(kx/r_a+1)^2} \quad (17)$$

CT is the coefficient of the fluid flow pushing power on the obstacle.

4. CFD Simulation

We simulate the rotational wake evolution generated by a solid obstacle in the fluid stream, such as a wind turbine rotor blade. We base the simulation on the k-ε model described above since the fluid operates in a turbulent regime. The simulation applies to variable fluid operational conditions and rotational wake angular speed, determining the wake performance, power efficiency, and energy saving. Because of the complex solution to the problem, we apply Computational Fluid Dynamics (CFD) to the mathematical treatment [16].

Since the obstacle geometry conditions the CFD simulation, it is necessary to define the geometrical obstacle characteristics [15]. We focus our study on a three-blade wind turbine rotor of 100 m in diameter, like the one shown in Figure 1 [17]. The obstacle type selection is due to the relevance of rotational wakes in wind farms.

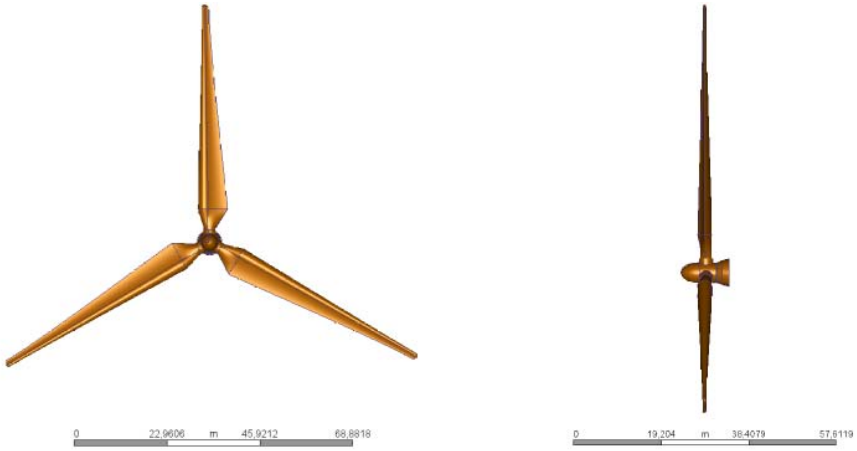

Figure 1: Front and Side View of The Obstacle's Geometry for The Rotational Wakes CFD Simulation in Turbulent Regimes Fluids

Before running the simulation, we develop a solid three-dimensional model of the obstacle's geometry using the 3D SolidWorks software library [18]. The simulation runs for a transient state in a turbulent regime.

The rotational speed, ω, depends on the fluid linear velocity, v, as in:

$$\omega = \lambda_r \frac{v}{r} \tag{18}$$

r is the distance to the virtual fluid stream duct axis, and λ_r is the angular to linear speed ratio.

Expressing Equation 18 in terms of rpm:

$$\omega(v) = \frac{30\lambda_r v}{\pi r} \tag{19}$$

If the fluid supplies the maximum power at the specific velocity v_o, considering v_i the speed at which the obstacle starts rotating, we have:

$$\frac{\omega}{v} = \frac{\omega_r}{v_o - v_i} \tag{20}$$

ω_r corresponds to the current rotation speed.

Now, replacing Equation 20 in Equations 18 and 19:

$$\omega_r = \lambda_r \frac{v_o - v_i}{r} \rightarrow (rad/s) \tag{21}$$

$$\omega_r = \lambda_r \frac{30}{\pi} \frac{v_o - v_i}{r} \rightarrow (rpm) \tag{22}$$

Equations 21 or 22 allow us to determine the speed ratio at any position of the rotational wake, provided we know the rotation speed and the fluid velocity at the maximum power and rotation start point.

Since a solid obstacle rotates at uniform angular speed, we can apply Equations 21 and 22 to the obstacle's tip, converting the equations into:

$$\omega = \lambda \frac{v_o - v_i}{R} \rightarrow (rad/s) \quad (23)$$

$$\omega = \lambda \frac{30}{\pi} \frac{v_o - v_i}{R} \rightarrow (rpm) \quad (24)$$

R is the radius of a virtual solid disk generated by the obstacle rotation.

Therefore, we can simulate the rotational wake initial state by simulating the obstacle rotation speed and vice versa. Figure 2 shows the evolution of rotation speed with fluid linear velocity.

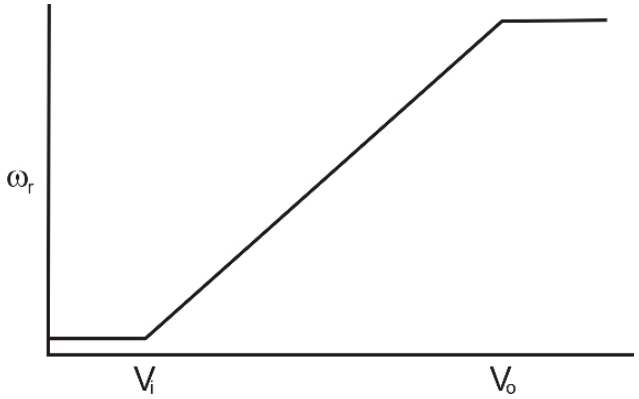

Figure 2: Evolution of Rotation Speed with Fluid Linear Velocity

The rotation speed steady state, below v_i and above v_o, depends on the λ-coefficient, which, on its way, depends on the system configuration. Table 1 shows the maximum and minimum value of ωr for variable λ values.

λ	5	6	7	8	9	10	11	12
ω_r (max)	2.9	3.4	4.0	4.6	5.2	5.7	6.3	6.9
ω_r (min)	9.5	11.5	13.4	15.3	17.2	19.1	21.0	22.9

Table 1: Minimum and maximum rotation speed (rpm) as a function of the λ-coefficient

Values in Table 1 correspond to a minimum incoming fluid velocity of 2 m/s and a variable maximum velocity between 5 m/s and 12 m/s.

For the simulation, we consider a square base prismatic space. The base surface is several times larger than the obstacle area. The prismatic space contours the obstacle with the vertical axis aligned with the fluid stream, one-twelfth of the vertical axis length upstream, and eleven twelfths downstream to ensure the rotational wake develops (Figure 3).

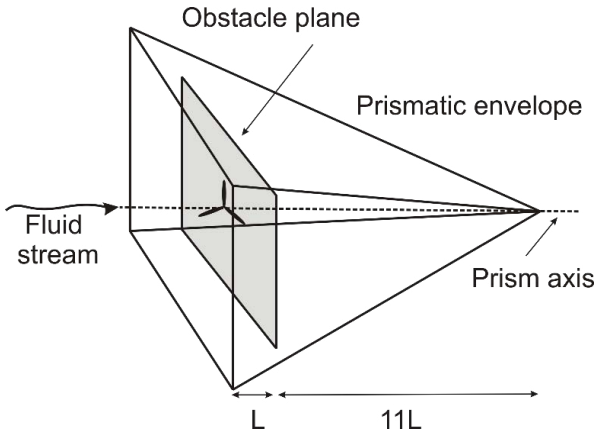

Figure 3: Schematic view of the geometrical representation for the CFD simulation

As boundary conditions, we impose vo as the fluid's incoming velocity at the entering surface, the prism base, and zero-gauge pressure at the prismatic space vertex. We impose a symmetry condition in the lateral prism faces, with the CFD program cloning the simulation space for every opposite face. As for the tridimensional meshing, the CFD program automatically divides the space into segments of appropriate length to solve the k-ε model equations; the segment's length reduces as we move from the base to the vertex of the prism. On the other hand, the meshing diminishes the size of every cell near the obstacle to avoid divergences in the problem solution. In the obstacle plane, we assume the rotation speed remains constant for specific fluid velocity, as shown in Figure 2.

Since the system operates in a transient state, there is no numerical solution but an approach representing a quasi-steady state. This is due to the rotational movement that generates a velocity fluctuation, forcing the wake shape to change in the obstacle nearby. Nevertheless, far away from the obstacle, the wake is completely developed, and the turbulent kinetic energy stabilizes; at this point, it is unnecessary to continue obtaining information from the system since the fluid velocity components oscillate around a defined value.

We obtain the values by inserting planes at different distances from the prism base toward the downstream direction. We add a plane parallel to the simulation faces at the center to get the velocity profile along the axis, considering the rotational wake is symmetric.

5. XZ Plane Results

We show the results in the XZ plane for the higher probabilistic fluid velocity and rotation speed according to the statistical distribution. Figures 4 and 5 show the simulation results for fluid velocity of 8 and 9 m/s and a rotation speed of 11 rpm. The parameter D, in the X and Z axis, corresponds to the diameter of the virtual solid disk representing the obstacle circular convolution.

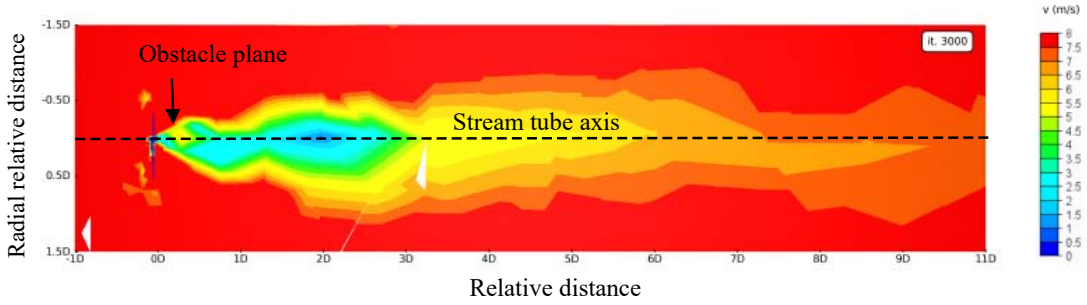

Figure 4: XZ plane rotational wake evolution simulation results for fluid velocity 8 m/s

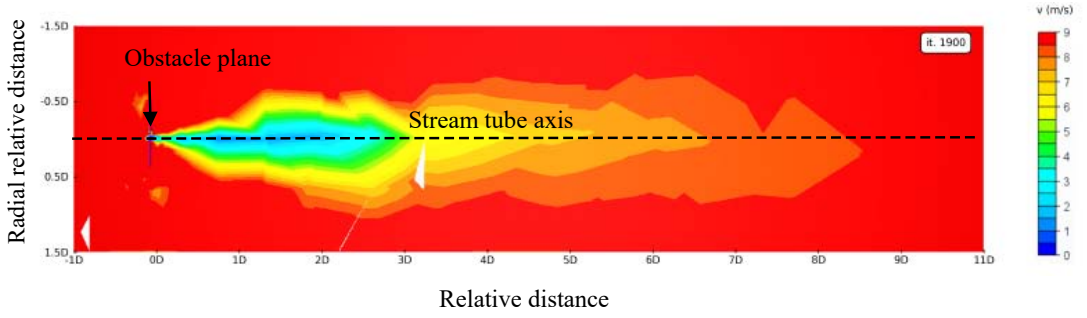

Figure 5: XZ plane rotational wake evolution simulation results for fluid velocity 9 m/s

We notice that the rotational wake evolution profile for the fluid velocity of 8 and 9 m/s is similar, confirming the Gaussian distribution assumption for the cross-section wake speed profile. On the other hand, the rotational wake is rather symmetric regarding the stream tube axis, indicating the wake evolution is uniform along the fluid stream.

Analyzing the rotational wake evolution for the two tested cases, we notice that the wake is not developed for the fluid velocity of 8 m/s; however, for the case of 9 m/s, the wake vanishes for a relative distance of 8.5 D. These two cases correspond to the fluid velocity threshold for which the turbulence evolves from a non-developed wake to a developed one.

Additional simulations showed that the rotational wake is less developed for lower fluid velocities, vanishing at a shorter relative distance for higher speeds. Figures corresponding to these simulations are not included to save space. On the other hand, we correlated the relative distance and the wake velocity at which the wake vanishes, resulting in the following drawing (Figure 6).

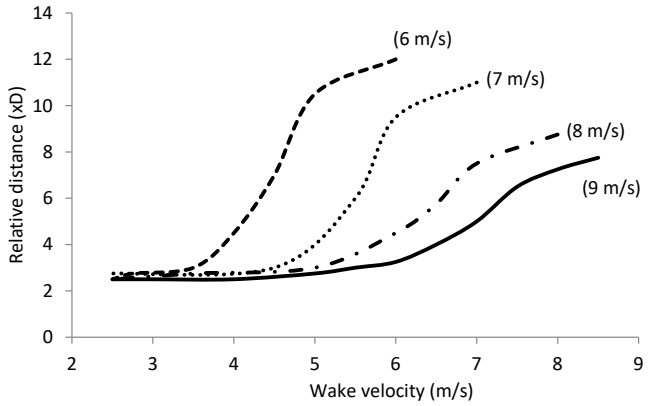

Figure 6: Correlation between the relative distance and wake speed for the rotational wake vanishing at various fluid velocities

The label for every curve corresponds to the fluid velocity.

We observe that the evolution of the relative distance at which the wake vanishes with the wake speed maintains a similar trend, smoothing as the fluid velocity increases. The analysis shows that the maximum variation in the wake evolution occurs in the 62% to 86% wake relative velocity range, with negligible or moderate variation below and above this range.

The above analysis shows that the wake influence on the fluid stream is maximum in the relative velocity range up to 62%, drastically reducing its influence in the 62% to 86% range and progressively eliminating the influence in the 86% to 100% relative velocity range.

Analyzing the dependence of wake evolution on relative distance from the obstacle, we notice there are also three ranges: 0% to 31%, 31% to 86%, and 86% to 100%, showing a minimum, high, and moderate variation.

The analysis results show that the critical zone where the rotational wake influences the most on the fluid stream is the region where distance is below 30% of the obstacle's virtual diameter: we expect turbulent kinetic energy, which vanishes rapidly as the rotational wake moves away from the obstacle's plane. To verify this statement, we evaluate the turbulent kinetic energy by applying the CFD method to the proposed configuration.

Now, repeating the simulation process for the turbulent kinetic energy (TKE), we obtain

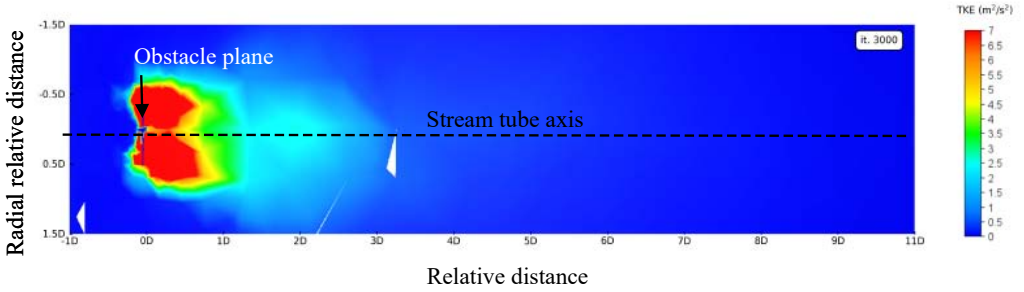

Figure 7: XZ plane turbulent kinetic energy evolution simulation results for fluid velocity 8 m/s

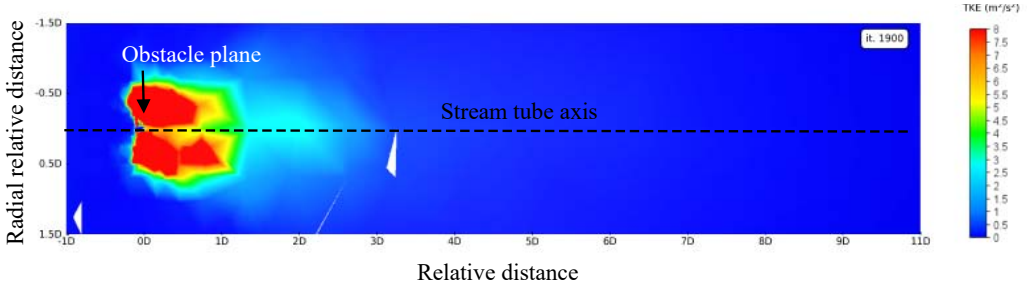

Figure 8: XZ plane turbulent kinetic energy evolution simulation results for fluid velocity 9 m/s

We observe that the turbulent kinetic energy extends to nearly 30% of the relative distance in both cases, confirming that the rotational wake's relevant influence occurs in a distance range from 0% to 30% of the obstacle diameter, drastically vanishing from this range on, as predicted by the previous wake evolution analysis.

According to this analysis, we should consider the region 0D-3D as the most important one for the fluid stream perturbation due to the rotational wake generation created by inserted obstacles in the fluid stream.

6. Wake Axis Simulation Results

We develop a simulation for the wake axis at variable incoming fluid stream velocities in addition to the wake cross-section. The wake and TKE evolution simulation results appear in Figures 9 and 10.

We notice that the wake speed matches the Jensen model from long distances on (Z>400 m), showing a speed Gaussian distribution (left side) independent of the incoming fluid stream velocity with a damping coefficient k=0.11. This evolution matches the trend shown in the XZ simulation for relative distances above 86%.

On the other hand, in the medium range (250 m < Z < 400 m), the wake speed follows a linear trend, matching the wake speed evolution in the range from 31% to 86%. Expanding this zone in Figure 6, we observe the linear variation for every incoming fluid stream with accuracy higher than 99% (Figure 11).

The closest zone to the obstacle's plane, where the rotational wake is more relevant, does not follow a specific pattern, confirming the importance of the turbulent effects in this section of the stream tube.

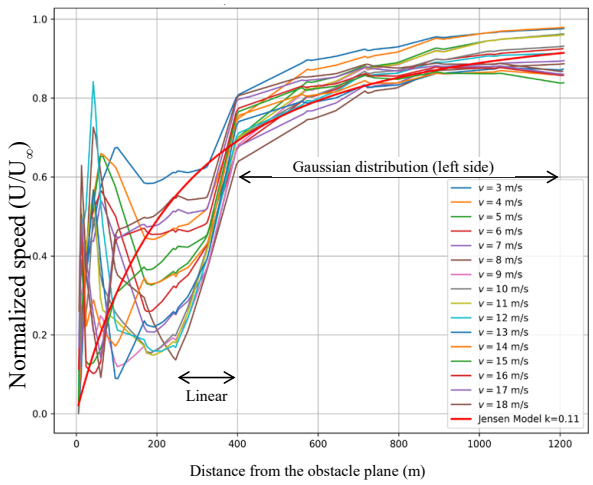

Figure 9: Normalized speed at the wake axis for variable incoming fluid stream velocity

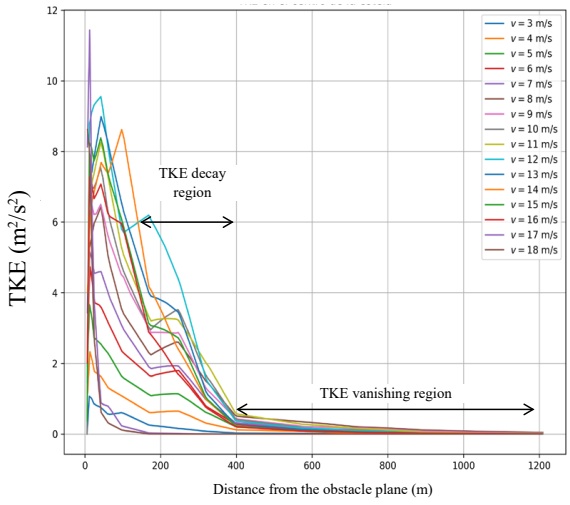

Figure 10: Turbulent kinetic energy at the wake axis for variable incoming fluid stream **velocity**

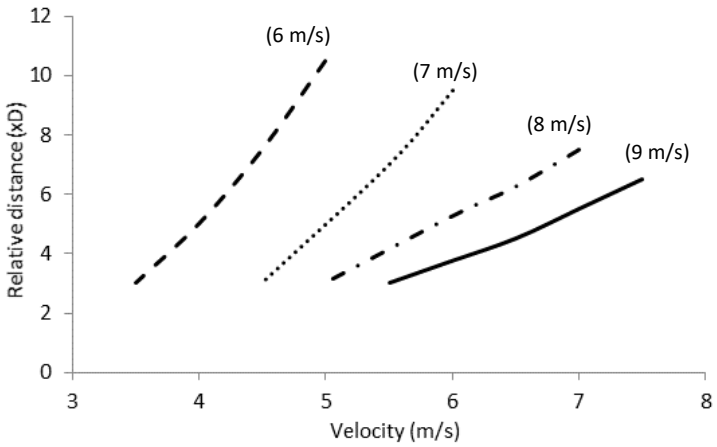

Figure 11: Correlation between the relative distance and wake speed for the rotational wake vanishing at various fluid velocities: wake speed center ranges from 31% to 86%

Regarding the turbulent kinetic energy (Figure 10), we observe that beyond Z=400 m (Z=4D), the TKE practically vanishes, confirming the situation at the XZ plane (Figure 8). In the region 1D<Z<4D, the turbulent kinetic energy shows a continuous decay, as reflected in the same zone for the XZ plane (Figure 8). Finally, the region 0D<Z<1D corresponds to the zone where the turbulent effects are more relevant with high fluctuations, similar to what we show in the XZ plane in Figure 8.

Retrieving data from Figure 6, if we correlate the relative distance at which the turbulent effects due to rotational wakes vanish and the incoming fluid velocity, we obtain the following expression:

$$Z = -1.6949U + 22.25 \quad (R^2 = 0.997) \qquad (25)$$

Applying Equation 25 for Z=0, the incoming fluid velocity is U=13.5 m/s, meaning that the turbulent kinetic energy is negligible above this velocity. This situation occurs because the rotation frequency provoked by the interaction between the incoming fluid and the obstacle matches the peak value shown in Figure 2, reducing the influence of turbulent effects to almost null value. A similar effect occurs at low fluid velocities due to the poor kinetic energy associated with the fluid stream. The minimum incoming fluid velocity for negligible turbulent kinetic energy should fulfill the condition: $Z=U_{TKE}=0$; therefore:

$$U_{\min} = \frac{22.25 - \frac{22.25}{1.6949}}{1.6949} = 5.4\ m/s \qquad (26)$$

The simulation concludes that the turbulent effects generated by rotational wakes correspond to the incoming fluid velocity range from 5.4 m/s to 13.5 m/s. Below the minimum and above the maximum threshold, the turbulent kinetic energy vanishes, with no further effects on the fluid stream.

We repeated the analysis for variable λ coefficient, from λ=5 to λ=12, according to values shown in Table 1, to determine the incoming fluid velocity range where the turbulent kinetic energy influences the fluid stream. Table 2 shows the results of the simulation.

λ	5	6	7	8	9	10	11	12
v (max)	14.20	13.50	13.20	13.00	12.90	12.85	12.80	12.75
v (min)	4.50	5.40	6.20	6.90	7.50	8.00	8.40	8.70

Table 2: Incoming fluid velocity range (m/s) for turbulent kinetic energy effects

We notice that the range amplitude diminishes as the λ coefficient increases, showing that the faster the obstacle rotation, the lower the turbulent kinetic energy effects.

If we draw the incoming fluid velocity range amplitude as a function of the λ coefficient, we obtain (Figure 12):

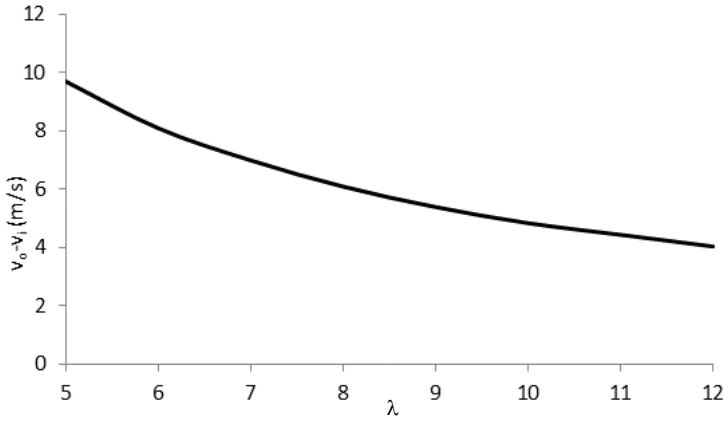

Figure 12: Incoming fluid velocity range amplitude as a function of the λ coefficient for the turbulent kinetic energy influence on the fluid stream

Correlating the velocity range amplitude and λ coefficient, we have:

$\Delta v=48.478\lambda^{-0.998}$ (R^2=0.9998) (27)

Equation 27 provides a practical algorithm to determine the incoming fluid velocity range for null turbulent kinetic energy on the fluid stream as a function of the λ coefficient.

If we correlate the minimum incoming fluid velocity to the λ coefficient, we obtain the following graph (Figure 13):

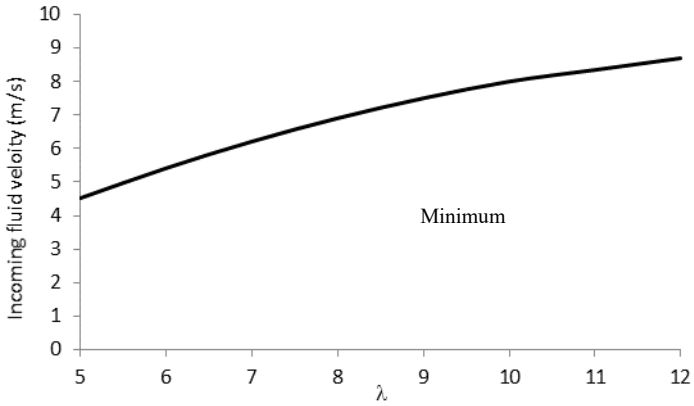

Figure 13: Minimum incoming fluid velocity as a function of the λ coefficient for the turbulent kinetic energy influence on the fluid stream

The minimum fluid velocity follows a potential law of the type:

$v_{min}=1.4022\lambda^{0.7509}$ ($R^2=0.9831$) (28)

We can determine the incoming fluid velocity maximum value by combining Equations 27 and 28.

7. Conclusions

The CFD technique is a practical tool for simulating the performance of turbulent kinetic energy generated by rotating obstacles in a fluid stream applying the k-e method.

The carried-out simulation shows that rotational wakes created by inserted obstacles in the fluid stream evolve with the fluid movement according to different performances. Near the obstacle, the rotational wake influence is maximal, with drastic changes in the rotation

speed and the fluid velocity. Far from the obstacle, the influence vanishes, and the rotational wake does not alter the fluid stream evolution. In the intermediate region, the rotational wake evolution follows a decreasing linear trend influence on the fluid stream.

The relative distance, computed in terms of the obstacle's diameter, D, where rotational wakes show the maximum influence, corresponds to the range 0D<Z<1.5D, followed by a region between 1.5D and 4D where the turbulence linearly diminishes until it vanishes from a distance 4D on.

Regarding the turbulent kinetic energy, the wake performance shows a similar behavior, with high values in the downstream vicinity of the obstacle and a linear decrease in the intermediate region, vanishing at high downstream distances from the obstacle.

The CFD simulation shows the relation between the incoming fluid velocity range amplitude and the λ coefficient, following a potential function relationship with near 100% accuracy. The power function correlation applies to the minimum incoming fluid velocity and the λ coefficient with more than 98% accuracy.

The incoming fluid velocity that generates rotational wakes influencing the fluid stream performance via turbulent kinetic energy moves between 4.5 m/s and 8.7 m/s for the minimum velocity value and between 14.20 m/s and 12.75 m/s for the maximum, in the λ coefficient operating range from 5 to 12.

References

1. Bagchi, P., & Balachandar, S. (2003). Effect of turbulence on the drag and lift of a particle. *Physics of fluids, 15*(11), 3496-3513.
2. Gustavsson, M. (2002). Fluid dynamic mechanisms of particle flow causing ductile and brittle erosion. *Wear, 252*(11-12), 845-858.
3. Wood, R. (2003). Aerodynamic drag and drag reduction. In 41st Aerospace Sciences Meeting and Exhibit (p. 209).
4. Temam, R. (2024). Navier–Stokes equations: theory and numerical analysis (Vol. 343). American Mathematical Society.
5. Doering, C. R., & Gibbon, J. D. (1995). Applied analysis of the Navier-Stokes equations (No. 12). Cambridge university press.
6. Málek, J., & Rajagopal, K. R. (2005). Mathematical issues concerning the Navier–Stokes equations and some of its generalizations. In Handbook of differential equations: evolutionary equations (Vol. 2, pp. 371-459). North-Holland.
7. Drazin, P. G., & Riley, N. (2006). The Navier-Stokes equations: a classification of flows and exact solutions (No. 334). Cambridge University Press.
8. Quartapelle, L. (2013). Numerical solution of the incompressible Navier-Stokes equations (Vol. 113). Birkhäuser.
9. Tu, J., Yeoh, G. H., Liu, C., & Tao, Y. (2023). Computational fluid dynamics: a practical approach. Elsevier.
10. Deng, X., Mao, M., Tu, G., Zhang, H., & Zhang, Y. (2012). High-order and high accurate CFD methods and their applications for complex grid problems. *Communications in Computational Physics, 11*(4), 1081-1102.
11. Barba, L. A., & Forsyth, G. F. (2018). CFD Python: the 12 steps to Navier-Stokes equations. *Journal of Open Source Education, 2*(16), 21.
12. Ghosh, A., & Pantaleón, C. (2013, November). Teaching Computational Fluid Dynamics Using MATLAB. In ASME International Mechanical Engineering Congress and Exposition (Vol. 56277, p. V005T05A024). American Society of Mechanical Engineers.
13. Iannelli, J. (2013). An exact non-linear Navier–Stokes compressible-flow solution for CFD code verification. *International Journal for Numerical Methods in Fluids, 72*(2), 157-176.
14. Cant, S. (2001). SB Pope, Turbulent Flows, Cambridge University Press, Cambridge, UK, 2000, 771 pp. *Combustion and Flame, 125*(4), 1361-1362.
15. Ge, M., Wu, Y., Liu, Y., & Yang, X. I. (2019). A two-dimensional Jensen model with a Gaussian-shaped velocity deficit. *Renewable Energy, 141,* 46-56.
16. Versteeg, H. K. (2007). An introduction to computational fluid dynamics the finite volume method, 2/E. Pearson Education India.
17. Onwubolu, G. C. (2017). Introduction to SolidWorks: A comprehensive guide with applications in 3D printing. CRC Press.
18. Shih, R., & Schilling, P. (2020). Parametric modeling with SOLIDWORKS 2020. Sdc Publications.